

# Steady and Unsteady Control of Nacelle Inlet Flow in Crosswind

Derek A. Nichols<sup>1</sup>, Bojan Vukasinovic<sup>2</sup>, and Ari Glezer<sup>3</sup>  
*Georgia Institute of Technology, Atlanta, GA 30332-0405*

Matthew DeFore<sup>4</sup> and Bradley Rafferty<sup>5</sup>  
*The Boeing Company*

## Abstract

The inlet flow of an engine nacelle model is investigated experimentally in the presence of cross flow that induces a complex, azimuthal separation pattern over the inner surface of the inlet's windward side. The evolution of the separation topology and its receptivity to flow control strategies are investigated in a state-of-the-art crosswind wind tunnel. Three fluidic-based control approaches are considered using steady jets and fluidically-oscillating jet actuators with and without internal feedback. Each of these approaches is tested using the same flow control configuration over a range of flow control parameters, inlet mass flow rates and cross flow speeds. While each actuation approach effects significant improvements over the base flow, the unsteady actuation methods generally outperform the steady method for the same actuation flow rate. Furthermore, it is found that fluidic oscillators are more effective at low speeds in the presence of internal feedback and at high speeds in the absence of internal feedback. Fluidic actuation in the absence of internal feedback reduces the distortion measure  $IDC_{max}$  by 55 and 50% at cross flow speeds of 30 and 35 kts, respectively, utilizing actuation mass flow rates that are lower than 0.3% of the inlet mass flow rate.

## Nomenclature

$C_q$	= $\dot{m}_j/\dot{m}_c$	$\dot{m}^*$	= $\dot{m}/\dot{m}_c$
$D$	= inlet throat diameter	$\dot{m}_j$	= mass flow rate jet
$f$	= suction blower operating frequency	$p_a$	= atmospheric pressure
$f_c$	= suction blower operating frequency at choking	$p_o$	= total pressure
$IDC$	= circumferential distortion index	$p_r$	= pressure ratio across actuator
$IDC_{max}$	= max circumferential distortion index	$U_o$	= crosswind speed
$IDC_{max}^*$	= $IDC_{max,choke}/IDC_{max,choke}(C_q = 0)$	$y$	= distance from wall
$\dot{m}$	= mass flow rate	$\theta$	= azimuthal coordinate
$\dot{m}_c$	= mass flow rate at choking		

<sup>1</sup> Graduate Research Assistant, AIAA Member.

<sup>2</sup> Senior Research Engineer, AIAA Member.

<sup>3</sup> Professor, AIAA Fellow.

<sup>4</sup> Aerodynamics Engineer, Boeing Commercial Aircraft

<sup>5</sup> Aerodynamics Engineer, Boeing Research & Technology, AIAA Member

## I. Background

Aircraft nacelles must be designed to comply with Federal Aviation Regulations (FARs) during all stages of the flight including ground operations, takeoff/landing and cruise (Maji et al., 2016; Chen et al., 2014). During flight operations close to the ground, the crosswind speed can be significant relative to the speed of the aircraft which can lead to flow separation and distortion at the engine face (Savelyev et al. 2014; Maji et al. 2016). The formation of a separation bubble on the windward side of the inlet can produce streamwise vortex shedding which can lead to compressor blade vibrations leading to possible blade damage or compressor stall (Übelacker et al., 2016; Radespiel et al., 2016). This separation bubble also decreases the effective cross-sectional area of the inlet which means that, for a fixed engine pressure ratio, the mass flow rate through the engine decreases (Übelacker et al., 2014). Some earlier investigations have also demonstrated the effect of separation hysteresis with varying intake speed which makes reattachment of the separation especially challenging (Hall and Hynes, 2006; Colin et al., 2007).

To accommodate flight in a crosswind during takeoff/landing, the nacelles must be oversized to withstand detrimental aerodynamic effects. This results in nacelles with increased weight and drag leading to lower overall efficiency during cruise which takes up the majority of the flight time. For smaller, FAR compliant nacelles to be designed, the inlet separation must be suppressed. This has been demonstrated using both passive aerodynamic bleed and active fluidically oscillating jets in wind tunnel experiments incorporating a nacelle in the presence of orthogonal crosswind up to 35 knots (Nichols et al., 2019, 2020). The present investigations further explore the differences in active flow control methods including steady CD nozzle jets and two fluidically-oscillating jet actuators with and without internal feedback.

## II. Experimental Setup and Flow Diagnostics

Experiments are conducted in a test facility at Georgia Tech designed specifically to investigate the physics of nacelle and crosswind interactions. This facility consists of two primary components: a model nacelle assembly and a cross flow wind tunnel (Figure 1). Both the inlet and cross flow blowers are independently controlled.

The nacelle model is mounted on a flow duct driven in suction by a computer-controlled blower. The nacelle model, which has a throat inlet diameter  $D$ , is attached to a diffuser followed by a long straight duct segment upstream of the blower's inlet. The duct is equipped with a probe for mass flow rate measurements placed between flow straighteners upstream and downstream. The blower exhaust air is driven into the room through two chilled water heat exchangers so that the ambient air temperature in the room is maintained at a prescribed level to within  $1^\circ\text{C}$ . The nacelle-duct assembly and the blower are supported on a frame that is movable using casters. This frame enables angular and axial adjustability about a pivot at the center of the tunnel test section. The angular adjustment serves to vary crosswind angle with respect to the inlet centerline (side slip). The nacelle height offset is always located midway between the test section floor and ceiling. In the present

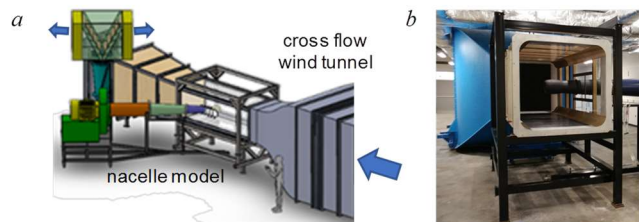


**Figure 1.** Schematics of the test facility (a) and the nacelle model installed in the test section (b).

investigation, the nacelle model is oriented normal to the cross flow direction while protruding halfway into the width of the test section.

The cross flow is generated by an open-return, low-speed wind tunnel having a contraction ratio of 10:1 that is driven by a computer-controlled axial blower. The tunnel’s square test section is optically transparent from three sides to enable flow visualization and optical diagnostics of the flow field about the nacelle’s inlet. The uniformity of the air speed within the test section was verified using velocity measurements at the test section exit plane in the absence of the nacelle model.

In addition to mass flow measurements, the two other main flow diagnostic tools used for the present investigation are total pressure measurements using a total pressure rake and particle image velocimetry (PIV) (Figure 2). The total pressure rake is located within the inlet where the fan face would nominally be located and consists of eight radial rakes of total pressure probes spaced in 45° increments.

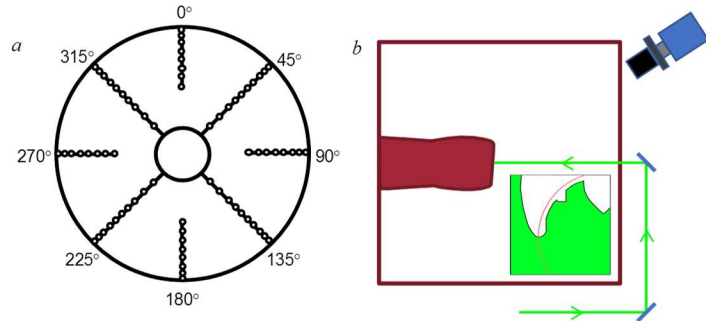


**Figure 2.** A rake of the total pressure probes (a) and the schematics of the PIV setup with an example field of view shown for reference (b).

The number of ports per rake alternate between eight and ten as shown in Figure 2a with a higher density of ports near the wall of the inlet to capture the growing boundary layer. The rake pressures are measured with a dedicated 96-channel pressure scanner with an uncertainty better than 1% of the time-averaged measurement. The inlet flow is also characterized with PIV using a *LaVision* system. Figure 2b illustrates the laser path into the inlet where the laser sheet intersects the windward lip of the nacelle. The camera is mounted above the inlet and is angled down to view the flow as it turns around and into the inlet. An example image is shown which includes schematics of the inlet surface for reference. The inset image illustrates the PIV field of view – a windward segment of the flow on the horizontal central plane ( $\theta = 270^\circ$ ).

The experimental testing procedure is designed to mimic the inlet condition during engine ramp-up/down on a runway which efficiently provides a sweep of mass flow rate data for a given crosswind speed (Figure 3). For a given configuration, the crosswind speed is fixed while the operating frequency of the suction blower is monotonically increased at a fixed rate up to a maximum-desired operating point and then monotonically decreased down to the starting operating point at the same rate. The commanded signal for the blower is shown with the black curve in Figure 3. The rates of increase and decrease are low enough to effectively create a quasi-steady variation of the inlet flow (Nichols et al., 2020). The change in the actual inlet mass flow rate is measured directly and is also shown in Figure 3. As seen in the plot, the mass flow rate eventually levels

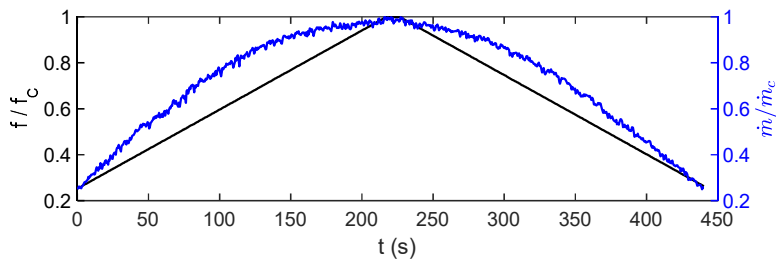


**Figure 3.** The commanded and realized ramp-up/down variation of the inlet mass flow rate.

eventually levels

off to a nearly constant value which corresponds to the choked condition (Nichols et al., 2019) through the inlet. By operating using this ramped procedure, instantaneous measurements of the mass flow rate and total pressures allow for a sweep of mass flow rates to be tested for a single condition while the quasi-steady ramp up/down rates ensure that each condition agrees with the corresponding time-resolved inlet mass flow rate and total pressure measurements.

### III. The Effects of Crosswind on Inlet Distortion

A comprehensive analysis of the intake flow and eventual separation topology was conducted by Nichols et al. (2019), who explored how the inlet separation topology changes with the intake speed while keeping a fixed crosswind speed, and vice versa. Nichols et al. (2020) further expanded this analysis by examining sweeps of the inlet mass flow rates instead of a discrete set of the operating conditions, mimicking the conditions that an aircraft nacelle would experience on the runway. As the engine ramps up on the runway, the engine pressure ratio increases. This causes the outer air to further accelerate over the inlet lip and turn into the inlet. Consequently, the near-surface flow begins to deviate from the surface contour, leading to the boundary layer thickening. This, in turn, leads to the higher momentum deficit near the surface and increases losses and distortion.

The rake total pressure measurements are utilized as a measure of the overall losses that would be imposed within the airplane engine. Additionally, the circumferential distortion index,  $IDC$  (see Colin et al. 2007) is one of many means of quantifying the total pressure distortion that an engine would face. It is derived by characterizing the circumferential heterogeneity of the total pressure distributions over the fixed radii, by examining the departures between each averaged total pressure and the minimum one along the full turn at the radius. Finally, the maximum  $IDC$  index over all of the considered radii for any given condition yields the maximum distortion parameter  $IDC_{max}$  that is used as the main distortion parameter. The default inlet geometry, without any flow control elements integrated into its modline (Figure 7a), was tested to establish a reference for the flow distortion in the presence and absence of cross flow. Figure 4 shows how the  $IDC_{max}$  parameter changes once a crosswind is introduced and how that profile exacerbates once the crosswind is increased from 25 to 35 knots,

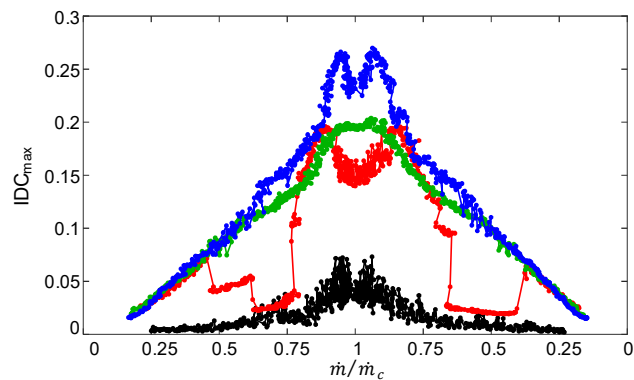


**Figure 4.** Circumferential distortion index over a sweep of mass flow rates for the crosswind speeds  $U_o = 0$  (●), 25 (●), 30 (●), and 35 (●) knots.

as measured during the described ramp-up/down procedure using the blower sweep described in Section II (Figure 3). In the absence of any cross flow, the total pressure deficit is compressed close to the surface, as the only source of any deficit is attributed to and confined to the boundary layer. These losses in total pressure, albeit confined to the near surface still amount to the levels of the  $IDC_{max}$  upwards of 0.05 or 5% at the peak of the mass flow rate sweep. Furthermore, the distortion measured for this case also appears to be unsteady in nature, although the sampling rates were insufficient to resolve the frequency content. Due to under sampling, unsteadiness appears as a scatter of the neighboring data points that spans roughly 5% at the highest flow rates, which points to the need for unsteady pressure measurements for full understanding of the unsteady

nature of the base flow at such flow conditions. Once a crosswind is introduced, the change in the  $IDC_{max}$  for each case in Figure 4 is rather dramatic. Looking first at the case of  $U_o = 25$  knots, the  $IDC_{max}$  profile starts off at a higher value than for the no crosswind case. This is because the baseflow starts off separated, which is reflected in both the increased total pressure losses and distortion. As the intake speed of the inlet increases, however, there are rapid discontinuities in the profile attributed to changes in the observed separation. In the range of  $0.6 < \dot{m}^* < 0.8$  during the ramp-up and  $0.65 > \dot{m}^* > 0.4$  during the ramp-down, the  $IDC_{max}$  briefly follows roughly the same path as the no crossflow case resulting from the flow attaching with no apparent separation. The flow eventually re-separates however and once again follows the same general trend as the other crosswind cases. Looking at the total curve for 25 knots, the effect of hysteresis is apparent from the asymmetry of the regions of separation and reattachment. The delayed reattachment on the ramp-down side is another example that the flow, once separated, tends to remain separated beyond the ramp-up separation point, which in turn induces a hysteresis in the flow response. It is noted that hysteresis is absent for the cases of a 30 and 35 knot crosswind because the flow remains separated during the entire mass flow rate sweep. Comparing the curves for the three crosswind speeds, the differences in the  $IDC_{max}$  between them is minimal for mass flow rate values of  $\dot{m}^* < 0.9$  for both the ramp-up and down. Still, some differences are noted at the highest flow rates. The distortion improves for the crosswind of 25 knots, remains constant for 30 knots, and continues to worsen for 35 knots. The 35 knot case exhibits the same reduction in the  $IDC_{max}$  at the highest flow rates as in the case of 25 knots. These reductions are likely due to the complex changes of the separation as the flow nears the choking condition that were observed in previous surface oil flow visualizations (Nichols et al., 2019). Overall, peak  $IDC_{max}$  values of about 0.14, 0.20 and 0.23 are reached for the maximum flow rates at  $U_o = 25, 30$  and 35 knots, respectively.

While the  $IDC_{max}$  plots convey much about how the distortion changes over time for the mass flow rate sweep, characteristic total pressure contours can better illustrate the actual total pressure deficit that is experienced at the fan face (Figure 5). These contours were generated at the choking condition ( $\dot{m}^* = 1$ ) for the 4 flow conditions discussed in Figure 4 (0, 25, 30, and 35 knots). Figure 5a shows the flow in the absence of cross flow and indicates almost no total pressure deficit,

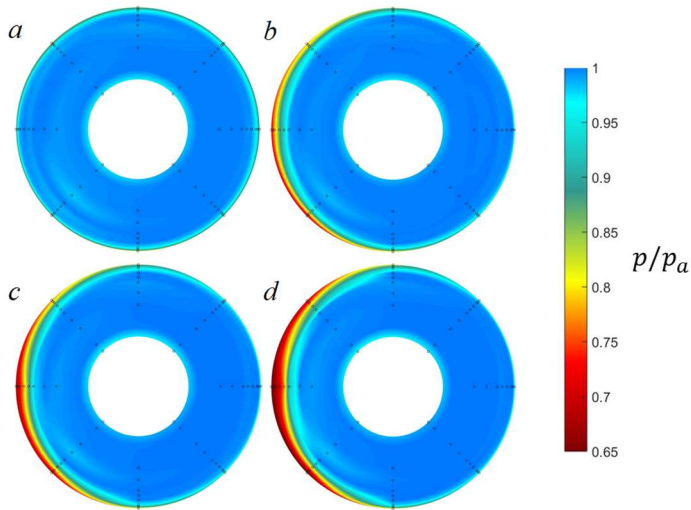


**Figure 5.** Base flow total pressure contour plots at the inlet normalized mass flow rate of  $\dot{m}^* = 1$  for the cross flow speeds  $U_o = 0$  (a), 25 (b), 30 (c) and 35 (d) knots.

besides very small nonuniformities near the wall. This is clearly expected as the outer air gets smoothly drawn into the inlet under this nominal condition. Once a crosswind is introduced, the contours show a quite different scenario. The windward side of the inlet is characterized by total pressure losses resulting from the ensuing flow separation. As the crosswind speed increases, these losses become more significant which agree with the  $IDC_{max}$  plots in Figure 4. This increase in the  $IDC_{max}$  is a result of an increase in not only the levels of the total pressure losses, but also the radial extent. The deficit is able to penetrate deeper into the inlet as the

crosswind speed increases. The losses are also relatively symmetric about the inlet with perhaps slight downward spreading as a result of the top-bottom asymmetry of the inlet. The separation in these areas of higher distortion is stronger and produces a larger effect on the flow field.

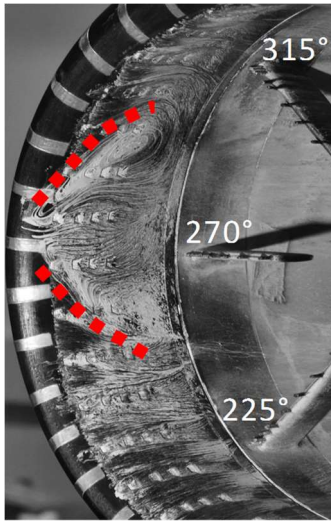


**Figure 6.** Surface oil-flow visualization of the windward inlet inner surface for  $U_o = 30$  knots and  $\dot{m}^* = 0.9$ . Separated domain bounds are marked by the dashed lines.

Both flow diagnostic techniques described previously utilize the total pressure rake, and as a consequence, they do not capture the inlet near-surface flow structure. Using surface oil flow visualization, the complex flow features along the inner windward surface are captured and the flow's behavior within and outside of the separated domain is elucidated. Figure 6 considers the flow through the inlet with speed  $\dot{m}^* = 0.9$  and crosswind speed of  $U_o = 30$  knots. This flow condition is chosen because of the high levels of distortion that it exhibits (Figure 4). As a reference, the azimuthal positions of the visible total pressure rakes are labeled on the image. From the oil traces (Figure 6), there is a clear separated domain in the form of a horseshoe pattern centered at  $\theta = 270^\circ$  and spanning  $245^\circ < \theta < 295^\circ$  which is bounded by two cell structures along its upper and lower boundaries. Above and below the separated domain, the flow exhibits non-axial traces along the wall. The flow does not regain axial alignment until approximately  $\theta = 225^\circ$  on the lower surface and  $\theta = 315^\circ$  on the upper surface where the flow eventually relaxes back to purely axial intake flow. More detailed analysis of the flow topology with the varying flow parameters is presented by Nichols et al (2019).

#### IV. Active Flow Control Approaches

Prior work by Nichols et al. (2020) demonstrated that active flow control can produce substantial benefits for nacelle flows in crosswinds. Current work builds on those earlier findings by exploring a potentially simpler steady-jet flow control approach, in addition to comparison between the previously utilized fluidic-oscillating jet

without the feedback loop (Nichols et al., 2020) and the fluidic oscillating jets driven by the feedback loop. Therefore, three approaches of active flow control are considered in the present study (Figure 7b-d), having all results compared to the uncontrolled 'smooth' inlet (Figure 7a). All three approaches incorporate an external air supply which pressurizes an internal plenum. Inside of the plenum, individual paths route to the control elements embedded into the inlet inner surface. A great care is taken that all the individual paths to the control elements are preserved among the three models. In addition, all flow control elements (the steady jet nozzle and the fluidic oscillating jet orifices) have the same rectangular throat dimensions and are positioned and oriented in the

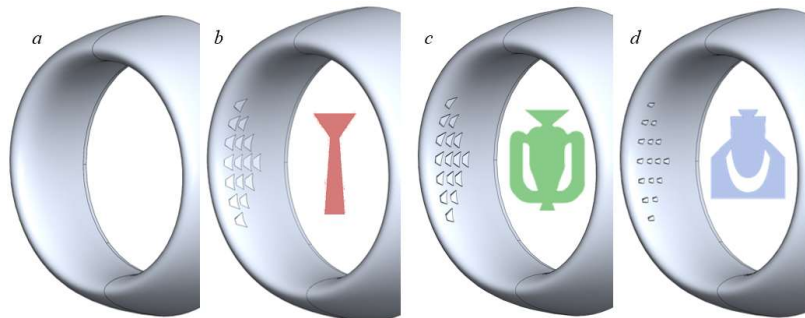


**Figure 7.** Flow control inlet test articles: default/smooth (a), and CD-nozzle (b) feedback-loop FO (c), and a non-feedback loop FO (d). Inset schematics illustrate individual flow control devices.

same way at each spatially discrete location. The flow control configuration of active individual flow control elements is chosen after the work by Nichols et al. (2020), which demonstrated a need for adjustable flow control patterns based on the changing flow topology due to the varying inlet speed and/or crosswind speed. As they showed that the preferable flow configuration at the highest intake speeds remains unchanged at either 30 or 35 knot crosswinds, that flow control configuration is selected for the present comparison among the three flow control components. As presented in more detail by Nichols et al. (2020) the flow control pattern is based on the separation domain topology (shown in Figure 6) and mimics the approximately inverted triangular shape of the separated domain marked in Figure 6.

The flow control elements, as illustrated in Figure 7b, utilize a steady converging-diverging (CD) nozzle. The CD nozzle design allows the flow to reach supersonic speeds upon exiting the inlet. Figure 7c illustrates a fluidic oscillator (FO) with a feedback loop, and Figure 7d indicates a FO model without a feedback loop. The non-feedback loop FO (Raghu, 2001) has been developed and tailored to various flow control applications over years at Georgia Tech, such as aero-optics (Vukasinovic et al., 2013), internal flows (Peterson et al., 2016), and propulsion (Burrows et al., 2019; Nichols et al., 2020), to name a few.

Although the throat dimensions were kept the same for all three flow control components, there is a distinction in their signatures on the inner surface of the inlet, as seen in Figure 7. Prior design of the non-feedback FO integration had a shallow diverging angle downstream from the actuator orifice, thus creating a relatively small cutout through the inlet inner moldline. A requirement for both the CD nozzle and feedback loop FO was to keep the continuation of the diverging nozzle profile past the orifice, thus creating a larger cutout through the surface, as illustrated in Figures 7b and c. Due to these different inlet surface modifications resulting from the different cutouts, the baseflow of the uncontrolled inlets with the integrated flow control elements were each compared to the smooth inlet for 30 and 35 knots (Figure 8). Comparing the  $IDC_{max}$  distributions over the entire mass flow rate sweep shows that each inlet follows a relatively similar trend with slight differences between them. The 30 knot sweeps (Figure 8a) show linearly increasing distortion measured until roughly  $\dot{m}^* = 0.85$ . At higher flow rates, the inlets experience sharper increases in distortion before eventually leveling out to a constant value once at choked flow. All plots are symmetric on ramp-up vs ramp-down indicating no hysteresis as the flow is consistently separated. For the 35 knot cases (Figure 8b), the profiles show more agreement

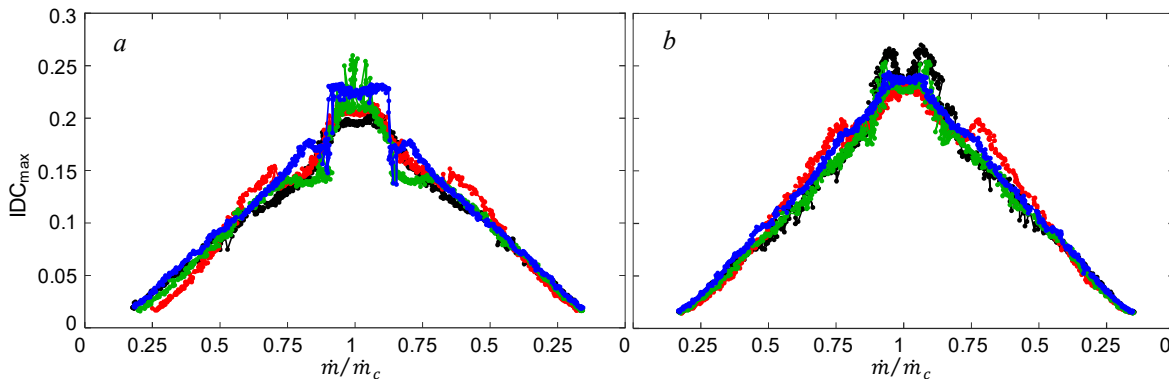


**Figure 8.** Comparing the circumferential distortion index over a sweep of flow rates for the four inlets of Figure 6: default/smooth (●), and CD-nozzle (●) feedback-loop FO (●), and a non-feedback loop FO (●) for 30 (a) and 35kt (b)

amongst themselves all reaching relatively the same  $IDC_{max}$  value at choking. While the modified inlet geometries due to the flow control integration exhibit some deviations in the base flow  $IDC_{max}$  evolution with the mass flow rate sweeps, they are still considered to be similar enough to be directly compared in terms of the controlled flow parameters. Alternatively, each of the controlled flow cases can be compared to its own uncontrolled state depicted in Figure 8.

Prior to the wind tunnel tests, bench test models for each of the flow control devices were manufactured and tested to characterize their performance in terms of the resulting mass flow rate through the individual component for a given pressure ratio, which is shown in Figure 9. For each of the three devices, there is initially a steeper rise in the device flow rate, with the rate of change somewhat decreasing for the remainder of the pressure ratios. These bench-test data suggest that all three components exhibit a similar functional relationship between the mass flow rate and the pressure ratio that drives the flow, but that the feedback-loop FO actuator exhibits the highest and the non-feedback loop FO the lowest pressure losses. It can be argued that a possible source of additional losses in the feedback loop driven FO are extended narrow flow passages in the loops and the additional incoming flow merging at the beginning of the loop.

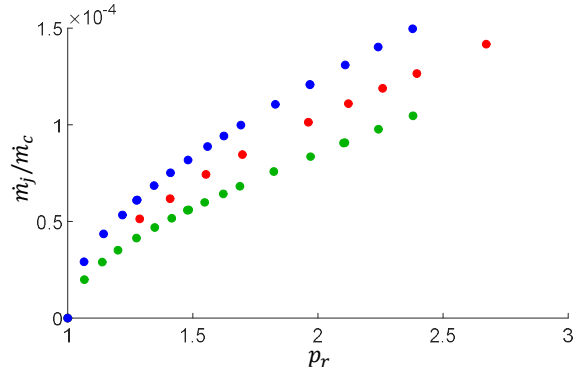


**Figure 9.** Fluidic-oscillating jet mass flow rate with the pressure ratio across the CD-nozzle (●) feedback-loop FO (●), and a non-feedback loop FO (●)

As stated previously, all three flow control approaches are tested on a single ‘triangular’ configuration of the flow control actuators (Figure 7b-d), as configured by the earlier work by Nichols et al. (2020). The flow control parameter, the jet flow rate coefficient  $C_q$ , is defined as a ratio of the total flow rate through the jets relative to the inlet flow rate at  $\dot{m}^* = 1$ . The effect of utilization of the CD nozzle steady jets in this flow control configuration is shown in Figure 10 for four different values of  $C_q$  (0.12%, 0.18%, 0.24%, and 0.27%) and are compared the inactive CD nozzle inlet. In addition, an inset plot shows the flow control configuration in Figure 10b, consisting of a triangular array of jets centered on the horizontal central plane of the windward

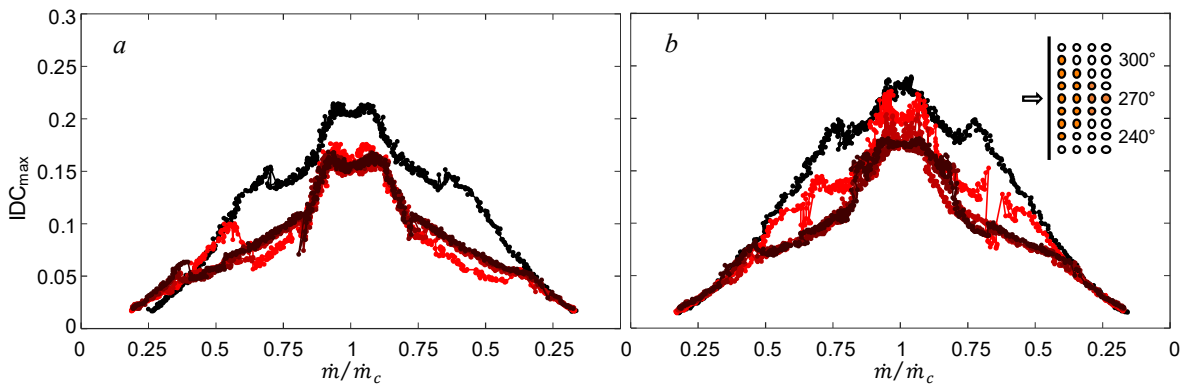


**Figure 10.** Comparing the circumferential distortion index over a sweep of flow rates for the uncontrolled (●) and controlled CD-nozzle using the inlayed configuration with a  $C_q$  of 0.12 (●), 0.18 (●), 0.24 (●), and 0.27% (●) for 30 (a) and 35kt (b).

side of the inlet ( $270^\circ$ ) and covering  $240^\circ < \theta < 300^\circ$ . Figure 10a shows the distortion values over the sweep of mass flow rates in a 30 knot crosswind. During the ramp-up sweep (Figure 10a), it is interesting that the lowest  $C_q$  control does not become effective until  $\dot{m}^*$  is ramped up to about 0.5, while the higher  $C_q$  cases initially are even slightly detrimental until they pull the distortion down at about  $\dot{m}^* = 0.35$ . Still, once the inlet flow rates are ramped up to the flow control design space ( $\dot{m}^* > 0.75$ ) all four flow control parameters seem to perform in a similar way. It can be argued that at the lower values of  $\dot{m}^*$ , when the radial extent of the separation is larger (Nichols et al., 2020), higher  $C_q$  is needed. This allows the flow to transition to a second mode of separation. Once in this mode, however, lower levels of  $C_q$  are preferred. Because of hysteresis, the flow can maintain this second mode of separation throughout the duration of the ramp-down for the flow rate sweep. The crosswind condition of 35 knots (Figure 10b) shows a similar initial trend. The highest values of  $C_q$  are able to reduce the baseflow distortion starting at about  $\dot{m}^* = 0.5$  allowing the inlet to transition to this second mode of separation. Once again, the favorable effect at the lowest value of  $C_q$  is delayed in this transition, this time until about  $\dot{m}^* = 0.8$ . Unlike the 30 knot case, however, the control by lowest value of  $C_q$  does not remain as effective at the highest inlet flow rates. There is a clear tier effect at the highest flow rates, with the further distortion reduction with an increase in  $C_q$  up to  $C_q = 0.24\%$  past which no additional benefit is attained with the increased  $C_q$ .

Analogous analysis is presented for the feedback-loop FO control in Figure 11. Here, however, even the lowest  $C_q$  is efficient at reducing distortion at the lowest inlet flow rates at 30 knots (Figure 11a). As a matter of fact, it takes higher inlet flow rates for the flow control at higher  $C_q$  to become effective, at about  $\dot{m}^* = 0.35$ . Regardless of the  $C_q$  level, all the flow control cases effect similar results thereafter, up to about  $\dot{m}^* = 0.85$ . However, the tiering effect noted in Figure 10 at the highest inlet flow rates becomes even amplified in the present case. The flow control at the lowest  $C_q$  rapidly weakens past  $\dot{m}^* = 0.8$ , bringing the distortion levels just below the base flow case at  $\dot{m}^* = 1$ . Similar, although much less severe trend is seen for  $C_q = 0.18\%$ , where the flow control effectiveness remains still notable at the highest inlet flow rates, reducing the peak distortion by about 20%. Finally, again similar to the steady jet analysis, there is no notable difference between the two highest  $C_q$  levels, indicating an optimal magnitude of  $C_q = 0.24\%$ . For the 35 knot sweeps (Figure 11b), the  $C_q$  level has no impact on the resulting distortion levels for

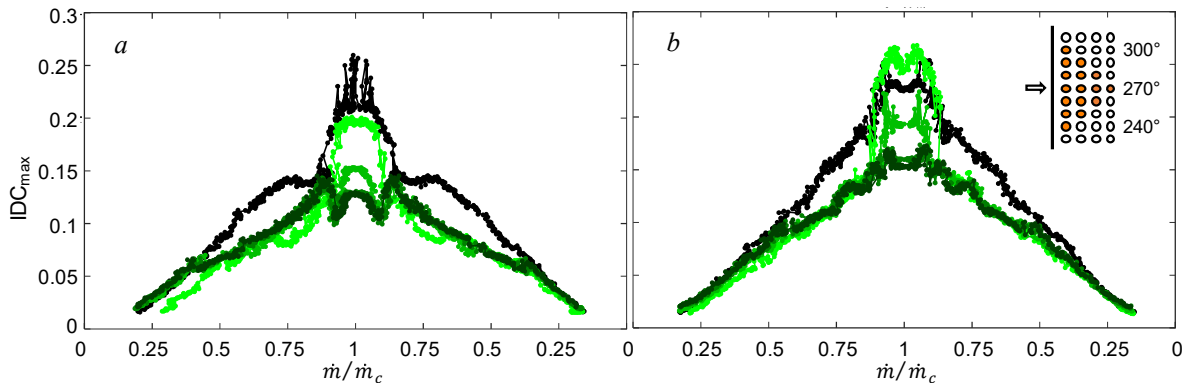


**Figure 11.** Comparing the circumferential distortion index over a sweep of flow rates for the uncontrolled ( $\bullet$ ) and controlled feedback loop FO using the inlayed configuration with a  $C_q$  of 0.12 ( $\bullet$ ), 0.18( $\bullet$ ), 0.24( $\bullet$ ), and 0.27% ( $\bullet$ ) for 30 (a) and 35kt (b) .

$\dot{m}^* < 0.9$ . However, the tiering noted at 30 knots (Figure 11a) is further amplified at the highest inlet mass flow rates. The flow controlled by the lowest  $C_q$  not only re-separates at the highest flow rates, but its associated distortion even surpasses that of the base flow. The flow control at  $C_q = 0.18\%$  does weaken at the highest flow rates but maintains the distortion levels below the base flow distortion, while the two highest  $C_q$  conditions do not show discernable difference. Therefore, it is notable that the same  $C_q$  level of  $C_q = 0.24\%$  is found to be the optimum level for both crosswind speeds. The other notable feature of the distortion evolution during the sweep up and down at the higher crosswind speed is that there is no observable hysteresis in the flow response. This is attributed to the inlet flow being not fully attached at any instance during the sweeps, but that the flow separation becomes rather suppressed, but not fully bypassed. Additionally, by comparing the results for the steady jets (Figure 10) and the feedback-loop driven FO jets (Figure 11), there is the same optimal flow control parameter that minimizes distortion expressed through  $IDC_{max} - C_q = 0.24\%$ .

Lastly, the non-feedback loop FO control, presented in greater detail by Nichols et al. (2020), is first assessed in an analogous manner in Figure 12. In the case of  $U_o = 30$  knots (Figure 12a), there is no notable effect of the flow control until the inlet flow rate is raised to about  $\dot{m}^* = 0.4$ . This is not surprising as this particular flow control configuration is designed to target the inlet flow separation at the upper range of flow rates (Nichols et al., 2020). Once the flow control becomes effective, contrary to the previous two cases shown in Figures 10 and 11, there is a clear delineation in its effectiveness over a range of  $C_q$  values. The lowest  $C_q$  control only slightly modifies the base flow distortion, while the other three have a significant effect. Moreover, there is a distinct tier for all of them at the highest inlet flow rates, where the distortion becomes progressively suppressed with the increasing  $C_q$ . Although no clear optimum  $C_q$  is attained within the tested range, there is a clear improvement in the distortion suppression at the highest  $C_q$  values, when compared to the steady and feedback-driven FO jets. A quite similar flow control effect is observed in the case of 35 knots crosswind (Figure 12b). The main difference is seen in slightly lesser effectiveness of the flow control in the absolute sense. The lowest  $C_q$  has even lesser favorable effect that practically completely diminishes at the highest inlet flow rates. It is interesting that increasing to  $C_q = 0.18\%$  effects the best distortion suppression at the midrange  $\dot{m}^*$ , but mimics the  $C_q = 0.12\%$  performance at 30 knots at the highest inlet flow rates – there is a very little

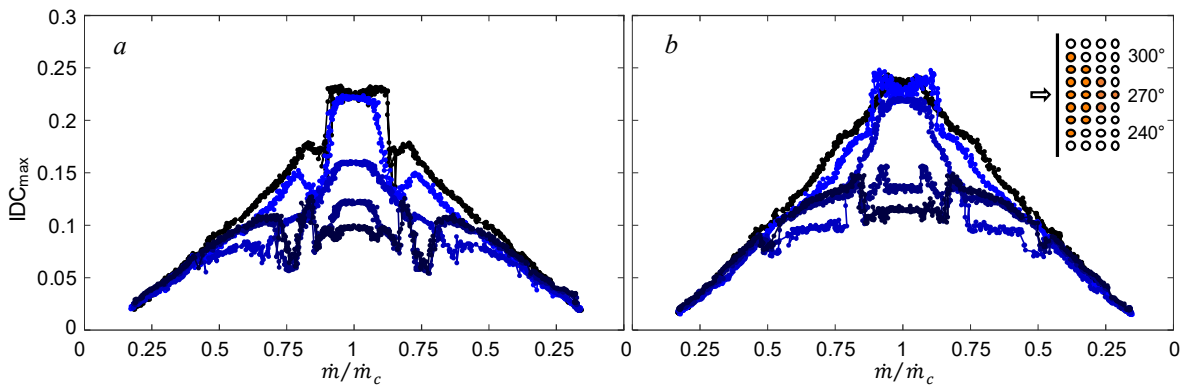


**Figure 12.** Comparing the circumferential distortion index over a sweep of flow rates for the uncontrolled (●) and controlled non-feedback loop FO using the inlayed configuration with a  $C_q$  of 0.12 (●), 0.18 (●), 0.24 (●), and 0.27% (●) for 30 (a) and 35kt (b) .

favorable effect at the highest flow rate. The effect of the flow control at the two highest-tested  $C_q$  values at  $U_o = 35$  knots is equivalent to their effectiveness at the lower crosswind speed. It is worth noting that due to the progressive increase in effectiveness with  $C_q$  increase throughout the tested range, no optimum flow configuration is reached and it can be argued that even better performance than that achieved for  $C_q = 0.27\%$  could be achieved with the further increase of  $C_q$ .

To summarize the flow control effectiveness of the three flow control approaches,  $IDC_{max}$  parameter change relative to the baseline level is shown in Figure 13 for the highest inlet mass flow rate  $\dot{m}^* = 1$ , and with the varying flow control parameter  $C_q$ . Effectiveness of the steady jets shows similar trends with increasing  $C_q$  regardless of the crosswind speed magnitude. There is an initial decrease in the distortion level, by about 20 – 25%, which is followed by saturation with the further increase in  $C_q$ . The flow control effect of both unsteady flow control approaches initially trails that of the steady jets, for the lowest levels of  $C_q$ . However, once the unsteady flow control starts to affect the inlet flow distortion, its rate of effectiveness rapidly increases. The feedback-driven FO control continues to decrease distortion levels past the minimum levels attained by the steady jets, until their effectiveness begins to level out at the highest  $C_q$  values, providing nearly 40% and 30% reduction of the base flow distortion at 30 and 35 knots, respectively. The difference, already observed earlier, in the non-feedback loop FO control is that no saturation levels are reached through the full  $C_q$  range. Therefore, this flow control approach attained reduction levels of about 55% and 50% at the highest  $C_q = 0.27\%$  for the crosswind speeds of 30 and 35 knots, respectively.

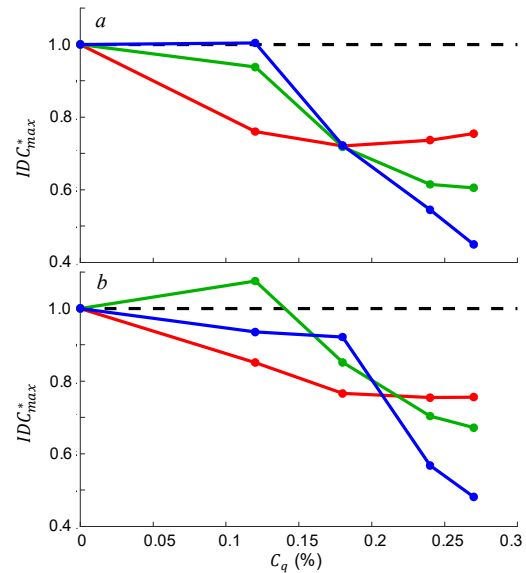


**Figure 13.** Comparing the circumferential distortion index at  $\dot{m}^* = 1$  as a function of  $C_q$  for the three flow control devices: CD-nozzle (●) feedback-loop FO (●), and a non-feedback loop FO (●) for 30 (a) and 35kt (b).

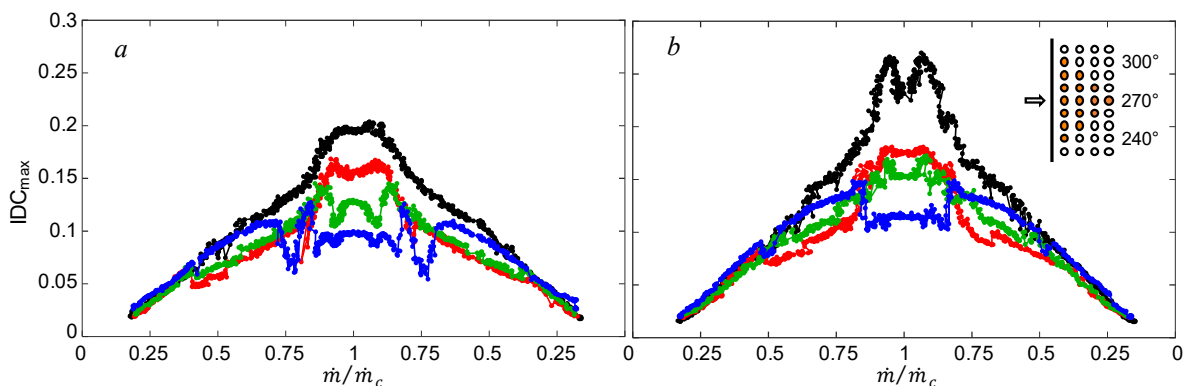


**Figure 14.** Comparing the circumferential distortion index over a sweep of flow rates for the four inlets of Figure 6: uncontrolled default/smooth (●), and controlled CD-nozzle (●) feedback-loop FO (●), and a non-feedback loop FO (●) using the inlayed configuration with a  $C_q$  of 0.27% for 30 (a) and 35kt (b).

Further comparison among all three flow control approaches is shown in Figure 14 over the full inlet mass flow rate sweeps and for the highest flow control parameter  $C_q = 0.27\%$ . None of the controlled cases indicate significant hysteresis, i.e., the flow control effect remains the same regardless of whether the inlet flow rate is ramped up or down. Although each of the flow control approaches significantly reduces the inlet flow distortion, particularly at the higher crosswind speed (Figure 14b), there are two distinct trends that are captured. First, over the lower mass flow rate range, effectiveness of the flow control approaches is reversed from their effectiveness over the targeted high flow rate range. In either the 30 or 35 knots crosswind-speed case, the largest suppression in distortion at the lower flow rates is recorded for the steady jets, followed by the feedback-loop driven FO jets, and the non-feedback FO jets which do not record any sizable affect until approximately half the maximum inlet flow rate. However, once the non-feedback loop FO jets becomes effective, they rapidly overtake the effectiveness of the other two approaches and clearly effect the largest distortion suppression at the highest inlet flow rates. It is interesting that the feedback loop-driven FO jets also surpass the steady jets effect at the higher inlet flow rates, thus completing the full inversion of the flow control effectiveness that is achieved at the inlet low flow rate regime.

## V. Characterization of the Non-Feedback FO-Controlled Flow Fields

The non-feedback loop FO, being the best performing flow control approach, is further characterized by assessing the inlet flow fields in the presence and absence of flow control. The PIV measurements, as outlined in Figure 2b, focused on the horizontal central plane on the windward side of the inlet ( $\theta = 270^\circ$ ) and spanning just past the inlet axis to focus on the flow turning into the inlet.

Figure 15 shows four such flow fields measured for 30 (Figure 15a and c) and 35 knots (Figures 15b and d), where the controlled (Figures 15c and d) is compared to the corresponding uncontrolled (Figures 15a and b) flows at  $\dot{m}^* = 0.9$ . The inlet surface is overlaid on the flow fields as a white mask for reference, with the red line denoting the lip apex. Besides the section of the conical central body, the upper section of the total pressure rake at  $\theta = 270^\circ$  is also seen in the view. The flow fields are presented by the sub-sampled equidistant mean velocity vector fields with the mean in-plane vorticity color raster plots. Both base flow fields (Figures 15a and b) indicate that the flow drawn along the outer nacelle into the inlet turns past the lip apex but begins to separate shortly thereafter. The

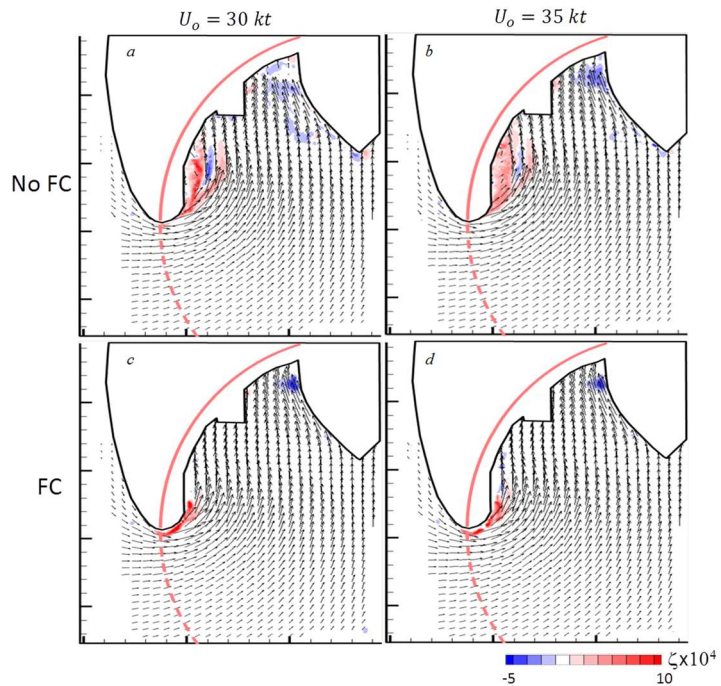


**Figure 15.** PIV for the uncontrolled default/smooth and controlled non-feedback loop FO using the flow control configuration in Figure 8 for the inlet mass flow rate  $\dot{m}^* = 0.9$  and crosswinds of 30 and 35kt. Schematics of inlet surface are shown for reference.

resulting shear layer is marked by strong vorticity concentrations and extends through the whole streamwise extent captured by the PIV measurements. Besides this prominent feature of the flow separation, the rest of the flow field indicates a gradual flow relaxation towards the axially drawn flow towards the central body. In addition, most of the captured flow, outside of the separated region close to the inner windward surface, becomes fairly axially aligned a short distance downstream from the inlet face. The main difference captured in the controlled flows is clearly seen along the windward inner surface (Figures 15c and d). Axial positions of the four active jets are marked on these plots for reference. Essentially, the most upstream jet is located at approximately the point of the base flow separation, and it is seen that all of the jets act in a sequence to attach the flow and keep it attached. Instead of the separated base flow, the controlled flow makes a full turn along the windward surface. The vorticity is now concentrated on only the front lip of the inlet indicating that the surface boundary layer thickens as the inlet flow turns and accelerates around the lip. This vorticity quickly dissipates as the flow is drawn into the inlet and interacts with the active jets near the wall in this region. A closer look at the rest of the flow field across the inlet face indicates that the local separation suppression has a far-reaching effect across the windward inlet face. The flow angularity is affected across the inlet in a way that the whole intake flow realigns better with the axial inlet orientation.

## VI. Conclusions

The present experimental investigations consider a nacelle inlet flow in crosswind and three flow control approaches for mitigation of the adverse effects of flow separation. Experiments are conducted in a nacelle cross flow facility in which a nacelle model operating in suction is placed in a wind tunnel providing the cross flow, such that the nacelle attitude is normal to the oncoming flow. The test conditions are designed to mimic engine ramp up and down by varying the inlet mass flow rate at a given (preset) crosswind speed. While multiple crosswind speeds have been tested, the present study focuses primarily on cross flow speeds for which massive azimuthal separation cells were observed by Nichols et al. (2019) namely,  $U_o = 30$  and  $35$  knots. Three fluidic-based control approaches are considered using steady jets and fluidically-oscillating jet actuators with and without internal feedback where all actuators share the same orifice dimensions. Each group of jets is distributed in the same flow control configuration, based on the optimal flow control configuration proposed by Nichols et al. (2020) for the highest inlet flow rates and crosswinds of  $30$  and  $35$  knots. In addition, rectangular orifice dimensions are preserved across all flow control components. The flow control input by each jet, measured as  $C_q$  per jet, is kept constant among all the three flow control components. Furthermore, as the total number of active jets is also kept constant, the total  $C_q$  is preserved as well.

It was found that each of the flow control approaches has a significant effect on the flow distortion reduction, which generally decreases with an increase in the flow control parameter  $C_q$ . Steady jet flow control typically outperforms both fluidically-oscillating jet configurations at low inlet flow rates. However, as the inlet flow rate is ramped up to the targeted peak rates, there is a switch in the effectiveness, such that the steady jet flow control is the least effective. Interestingly, both the steady jet and the feedback-driven FO control exhibit saturation in terms of the distortion reduction with the increase in  $C_q$ , while the non-feedback-driven FO control progressively increases in effectiveness over the whole  $C_q$  range. Consequently, this flow control approach attains distortion reduction of about  $55\%$  and  $50\%$  at the highest  $C_q = 0.27\%$  for the crosswind speeds of  $30$  and  $35$  knots, respectively. Due to the saturation at the highest  $C_q$  values, feedback-driven FO control

achieves nearly 40% and about 30% reduction of the base flow distortion at 30 and 35 knots, respectively. Lastly, steady jets' effect at the high inlet mass flow rate saturates through the midrange  $C_q$  values, resulting in only 20 – 25% improvement over the base flow distortion.

Additional flow characterization by PIV within the central horizontal plane indicates that the flow control applied by the non-feedback-driven FO control does suppress the local flow separation of the base flow, which is the major source of the total pressure deficit and distortion at the crosswind speeds of 30 and 35 knots. This local flow attachment by the flow control has a far-reaching effect on the bulk flow as well, since most of the turning bulk flow realigns closer to the axial intake direction in the controlled flows. The PIV-measured flow fields also suggest that the streamwise-distributed flow control jets act in tandem, as the base separated flow does not become fully attached immediately downstream from the most upstream jet, but a rather compound effect of the two upstream jets brings the flow to attachment, which is further maintained through the measurement's domain by the action of the two downstream jets.

Regardless of the flow control component that is utilized, it should be emphasized that the optimal spatial configuration of such components would depend on the base flow separation topology for a given set of the driving parameters (characteristic scales of the inlet and the crosswind flows). As discussed by Nichols et al. (2019), these separation topologies can be quite complex and vary from one regime of the operating parameters to another.

## Acknowledgment

This research has been supported by The Boeing Company, Georgia Tech, and the National Science Foundation Graduate Research Fellowship under Grant No. DGE-1650044.

## References

- Burrows, Travis J., Vukasinovic, Bojan, Lakebrink, Matthew T., Mani, Mortaza, and Glezer, Ari. 2019. "Control of Flow Distortion in Offset Diffusers Using Trapped Vorticity." *International Journal of Heat and Fluid Flow* 75 (November 2018): 122–34. <https://doi.org/10.1016/j.ijheatfluidflow.2018.11.003>.
- Chen, Jingjing, Wang, Zhonglin, Wu, Yadong, and Wang, Anjenq. 2014. "Nacelle , Air Intake Aerodynamic Design And Inlet Compatibility." In *Proceedings of the ASME 2014 Gas Turbine India Conference GTINDIA2014*.
- Colin, Y, Aupoix, B, Boussuge, J F, and Chanez, P. 2007. "Numerical Simulation and Analysis of Crosswind Inlet Flows at Low Mach Numbers." *Proceedings of the 8th International Symposium on Experimental and Computational Aerothermodynamics of Internal Flows*, no. ISAI8-0058.
- Hall, Cesare a., and Hynes, Thomas P. 2006. "Measurements of Intake Separation Hysteresis in a Model Fan and Nacelle Rig." *Journal of Propulsion and Power* 22 (4): 872–79. <https://doi.org/10.2514/1.18644>.
- Maji, Frane, Efraimsson, Gunilla, and Reilly, Ciarán J O. 2016. "Potential Improvement of Aerodynamic Performance by Morphing the Nacelle Inlet." *Aerospace Science and Technology* 54: 122–31. <https://doi.org/10.1016/j.ast.2016.04.006>.
- Nichols, Derek A., Vukasinovic, Bojan, Glezer, Ari, DeFore, Matthew C., Rafferty, Bradley, and Palacios, Francisco D. 2019. "Characterization and Control of Nacelle Inlet Flow in Crosswind." *AIAA Aviation*, no. June. <https://doi.org/10.2514/6.2019-3685>.
- Nichols, Derek A., Vukasinovic, Bojan, Glezer, Ari, DeFore, Matthew, and Rafferty, Bradley. 2020. "Fluidic Control of Nacelle Inlet Flow in Crosswind." *AIAA Aviation*. <https://doi.org/10.2514/6.2020-2955>.
- Peterson, Curtis, Vukasinovic, Bojan, Glezer, Ari, Saripalli, Kondala R, and Packard, Nathan O. 2016.

- “Active Flow Control of Separation in a Branched Duct.” In *8th AIAA Flow Control Conference*. AIAA AVIATION Forum. American Institute of Aeronautics and Astronautics. <https://doi.org/doi:10.2514/6.2016-3771>.
- Radespiel, Rolf, François, Daniela Gisele, Hoppmann, David, Klein, Simon, and Scholz, Peter. 2016. “Simulation of Wing and Nacelle Stall.” *AIAA SciTech*, 1–20. <https://doi.org/https://doi.org/10.2514/6.2016-1830>.
- Raghu, Surya. 2001. Feedback-free fluidic oscillator and method. 6,253,782, issued 2001.
- Savelyev, A A, Mikhaylov, S V, and Zlenko, N A. 2014. “Aerodynamic Inlet Design for Civil Aircraft Nacelle.” *29th Congress of the International Council of the Aeronautical Sciences*, 1–10.
- Übelacker, Simon, Hain, Rainer, and Kähler, Christian J. 2014. “Flow Investigations in a Stalling Nacelle Inlet.” *17th International Symposium on Applications of Laser Techniques to Fluid Mechanics*.
- . 2016. “Flow Investigations in a Stalling Nacelle Inlet under Disturbed Inflow.” *Advances in Simulation of Wing and Nacelle Stall*. <https://doi.org/10.1007/978-3-319-21127-5>.
- Vukasinovic, B., Glezer, A., Gordeyev, S., Jumper, E., and Bower, W. W. 2013. “Flow Control for Aero-Optics Application Topics in Flow Control. Guest Editors J. P. Bonnet and L. Cattafesta.” *Experiments in Fluids* 54 (3). <https://doi.org/10.1007/s00348-013-1492-8>.